Demonstration of o-Ps Detection with a Cylindrical Array of NaI Detectors

Chelsea Bartram[1,*], Reyco Henning

Department of Physics and Astronomy, University of North Carolina, 120 E. Cameron Ave, Phillips Hall CB3256, Chapel Hill, NC 27599

Triangle Universities Nuclear Laboratory, Durham, NC, USA

Daniel Primosch

Department of Physics, University of Washington, 3910 15th Ave. NE, Seattle, WA 98195-1560

Abstract

Ortho-positronium (o-Ps), the triplet bound state of an electron and positron, is a promising system in which to search for new physics. O-Ps production and detection can be achieved with a tabletop setup, involving a ^{22}Na source, aerogel and a detector. We present our approach to o-Ps detection using the APEX array, which consists of 24 NaI(Tl) bars, arranged cylindrically. Our approach involves tagging on the 1.27 MeV gamma ray, a technique which is used in positron annihilation spectroscopy (PALS) [1]. We demonstrate the ability to tag with any one of the bars in the array. Using a NaI(Tl) array of high angular coverage (75%) with this technique provides many benefits. This method provides some advantages over tagging on the positron directly insofar as it minimizes the amount of material inside the source holder and simplifies the design of the DAQ. This has potential applications to CP- and CPT-violation searches in o-Ps.

1. Introduction

Positronium (Ps) is a neutral bound system of an electron and a positron that self-annihilates into gamma-rays via the electromagnetic interaction. It is a purely leptonic system that is well-understood and theoretically simple,

*Corresponding Author
Email address: chelsb89@uw.edu (Chelsea Bartram)
[1]Now at University of Washington

i.e. there are no complex QCD corrections needed. It is completely described by quantum electrodynamics (QED) with extremely small weak force corrections [2].

Positronium can exist in either a CP-odd spin singlet state ($^1S_0$), called para-positronium (p-Ps), or a CP-even spin triplet ($^3S_1$) state called ortho-positronium (o-Ps). Because QED requires C-conservation, the p-Ps state can only decay into an even number of photons, whereas the o-Ps can only decay into an odd number of photons greater than or equal to three [3]. The o-Ps state is much longer-lived in vacuum (142 ns vs 125 ps) [4–9] than the p-Ps state due to phase space considerations and the additional factor of α (fine-structure constant), making it more sensitive to admixtures of new interactions [10–12].

Another feature of this leptonic system is the relative simplicity of generating it in the lab. A common technique for generating o-Ps is to combine a positron emitting nuclide, such as ^{22}Na, with aerogel [13, 14]. Positrons emitted into the aerogel will form positronium, which decays into gamma rays that can be detected. One possibility of using this setup is to search for CP- and CPT-symmetry violating interactions that manifest in angular correlations between the gamma rays emitted from o-Ps decay. Such searches were first proposed in 1988 [10]. A search for CP-violation would involve the measurement of a CP-violating observable, such as $(\vec{S}\cdot\vec{k_1})(\vec{S}\cdot\vec{k_1}\times\vec{k_2})$, where S is the spin of the o-Ps, $\vec{k_1}$ is the momentum of the highest energy gamma ray in o-Ps decay, and $\vec{k_2}$ is the momentum of the second highest energy gamma ray. Likewise, a search for CPT-violation would involve the measurement of a CPT-violating observable, such as $(\vec{S}\cdot\vec{k_1}\times\vec{k_2})$. The signature of symmetry violation in both cases is a non-zero value for the asymmetry term, $A = (N_+ - N_-)/(N_+ + N_-)$, where N_+ is the number of times the respective (CP- or CPT-violating) observable is positive, and N_- is the number of times the respective observable is negative. Previous such searches have yielded asymmetries consistent with zero [15, 16], yet efforts to improve the limits continue. For example, one recent effort in this regard uses a reconstituted PET (positron emission tomography) scanner to perform a similar search [17].

O-Ps detection requires a lifetime measurement which can be obtained by measuring the time interval between the positronium formation and its decay. Past CP- and CPT-violation searches in o-Ps [15, 16] used the positron emission time as a proxy for the o-Ps formation time by tagging on the positron with a thin piece of scintillator. This works because the time between positron emission and o-Ps formation is negligible (on the order of several picoseconds, using positron energies and implantation depths described in [11]). Tagging on the positron requires an additional level of complication to these experiments, as scintillator material must be placed between the aerogel and source. Gamma ray scattering from this extra material can lead to systematic effects in experiments that measure the angular correlations between the emitted gammas, such as search for CP- or CPT-violation. Light from the scintillator must also be piped via optical fiber to a PMT, the signal from which is then used to trigger the DAQ. This adds an extra level of complication to the DAQ system.

Using the APEX array [18], a 24-bar NaI(Tl) detector located at Triangle Universities Nuclear Lab (TUNL), we designed and built a system that uses an alternative approach. While the technique of tagging on the 1.27 MeV gamma ray has been used in PALS [1], we have demonstrated the technique with a segmented NaI array (APEX) that can use any of its 24 bars to detect the start signal. This minimizes the amount of material in the region of the source holder and decreases the complexity of the DAQ. These two features may prove advantageous in CP- and CPT-violation searches.

2. Instrumentation and Design

2.1. Principle of Operation

We positioned a $10\,\mu$Ci ^{22}Na source at the center of a cylindrical array of 24 NaI(Tl) bars. Positrons emitted from one side of the source were moderated in a cylinder of hydrophobic silica aerogel to form o-Ps (see Fig. 1). According to the $V-A$ theory of weak interactions, the positrons were initially polarized along their momenta according to $\vec{P} = \vec{v}/c$ [19]. The o-Ps, in turn, acquired the spin of the positron, with some probability. About 67% of positrons emitted from the front-facing side of the source are polarized in the positive z-direction [15]. 90% of the positrons are not depolarized by aerogel interactions. Finally, about 67% of the remaining positrons transfer their polarization to the o-Ps [15]. Since the aerogel is only on one side of the source, the positrons and o-Ps had a net polarization pointing away from the source. Positrons traveling in the opposite direction were stopped by an aluminum backing. Phase space considerations and momentum conservation required that o-Ps decayed primarily into 3 coplanar gamma-rays, denoted $\vec{k_1}$, $\vec{k_2}$, $\vec{k_3}$ in order of highest energy to lowest. Most of the gamma rays interacted in the NaI(Tl) crystals and the resulting scintillation light was detected by PMTs at the ends of each bar. Position reconstruction was accomplished using the relative pulse amplitudes from the two PMTs and the locations of the bars. The start signal was provided when the 1.27 MeV gamma, emitted in the decay of the ^{22}Na nucleus, interacted in a NaI(Tl) bar. Charge pulses and their timing information were collected by VME-based CAEN Modules.

2.2. Source, Source Holder, and Supports

The source was a model POSK-22 provided by Eckert & Ziegler Isotope Products, Inc [20]. Its physical diameter was 12.7 mm with an active diameter of 5.08 mm. The $10\,\mu$Ci ^{22}Na activity was deposited between two layers of $7.2\,\mathrm{mg/cm^2}$ polyimide and sealed with epoxy. The delrin source holder (see Fig. 1) contained the source, backing, and aerogel moderator. A retaining cap held the source flush against the aerogel. An aluminum backplate absorbed positrons emitted in the opposite direction from the aerogel.

The source holder was inserted into a carbon fiber tube (inner diameter of 0.75 inches; wall thickness of 0.035 inches) which was mounted in the center of the APEX array using an external support structure. This structure enabled the alignment of the positronium source at the center of the array. The holder was held in place in the center of the carbon fiber tube with delrin retaining pins (see Fig. 1). The support structure was suspended from an aluminum channel

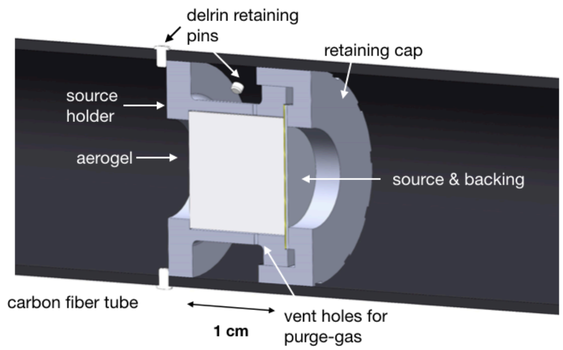

Figure 1: Cross section of the carbon fiber tube containing the source holder (gray), source, backing and aerogel moderator (white).

that was mounted on top of the detector (see Fig. 2). In the front and back of the array, the holder was clamped into two adjustable poles affixed to the channel via threaded collars that provided 1.0 mm alignment in the z-direction. We observed that the z position alignment was compromised slightly by the fact that the carbon fiber tube could be somewhat compressed along its length. Four lateral alignment fixtures on either side of the channel in the front and back of the array enabled 0.5 mm positioning in the x-direction. The tube was continuously purged with dry nitrogen gas, which minimized so-called 'pick-off' annihilation and reduced quenching of o-Ps in the aerogel [21]. The holder had vent holes to enable purge-gas to flow through the aerogel.

2.3. APEX Array

The APEX array is a cylindrical, NaI(Tl) scintillator array, originally constructed for the ATLAS Positron Experiment (APEX) [18], that has been upgraded and reassembled for use in low-energy nuclear experiments at the Triangle Universities Nuclear Laboratory (TUNL) [22, 23]. APEX consists of 24 NaI(Tl) crystals of trapezoidal cross section. Each individual bar is of dimension $55.0 \times 6.0 \times 5.5$ (7.0) cm^3 (L $\times$ H $\times$ W (longer width of trapezoid) cm^3) and sealed in a 0.4 mm evacuated stainless steel encasement with quartz windows on either end. PMTs on both ends of each bar are optically coupled directly to

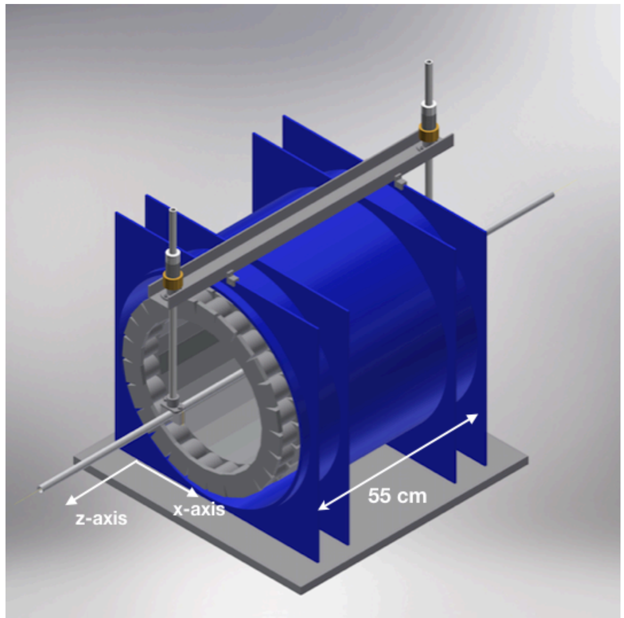

Figure 2: Rendering that shows the carbon fiber tube mounted inside the APEX array.

the quartz windows using Saint-Gobain BC-630. Hamamatsu R580 PMTs are used for 16 of the bars, and the Photonis XP2012B for the remaining 8 bars. With all bars fully operational and a source at the center of the array, the array has 75% of 4π angular coverage. The inner diameter of the array is 42.8 cm.

3. Data Acquisition System

The data acquisition system (DAQ) is shown in Fig. 3. The DAQ made use of the CAENV775 TDC and CAENV862 QDC cards in conjunction with CAENV812 Constant Fraction Discriminators (CFDs) to record the charge and timing information associated with each event [24]. The DAQ used three QDC cards, for a total of 96 QDC channels (32 per QDC), and one TDC card, for a total of 24 TDC channels (one per NaI(Tl) bar). All cards were mounted in a single VME crate. Though unnecessary for the purpose of o-Ps detection, the CAENV862 QDCs require individual gates in addition to a common gate. We chose to work with this as they were the only QDCs available.

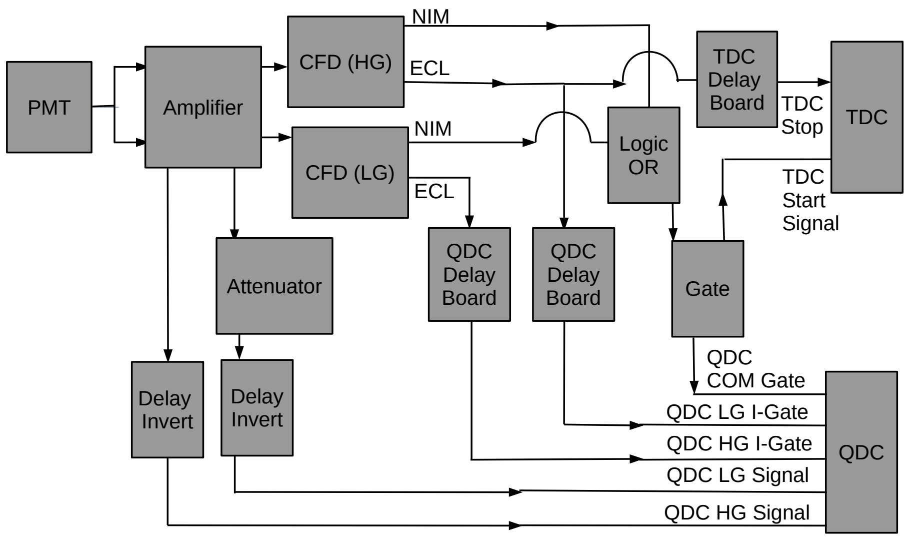

Figure 3: DAQ Schematic. Signals from a single PMT are split into high and low gain channels. The split signals are fed into an amplifier with two outputs per input. One such output triggers the CFD, which produces several digital control signals: the ECL and NIM gates for the QDC, and the start and stop signals for the TDC. The NIM output of the CFD is the OR of all the inputs, whereas the 16 ECL gates per CFD have a one-to-one correspondence with the input signals. The other output from the amplifier proceeds to the QDC via various passive electronics that alter the signal. The 'low' gain signal travels through a pi-pad attenuator circuit equipped with a capacitor to remove any DC offset. This board also performs an inversion of the signal necessary for the QDC. The 'high' gain signal travel through an identical setup, but without the attenuator. The trigger system and electronics pertaining to the other two QDCs are not shown for simplicity.

The output of each PMT was split in two via a lemo T before entering two separate input channels of an amplifier (NIM Model 776, Phillips Scientific). These two signals ultimately corresponded to what we refer to as the 'high and low gain channels'. The NIM amplifier has a voltage gain of 10 and produced two identical outputs for each input: one output provided the trigger pulse for the CFD and the other provided the signal input of the QDC. For the high gain channels, the signal which traveled from the amplifier to the QDC passed through a custom board which inverted and delayed the pulse via a TF200-5 (200 ns) delay chip. A capacitor on the board also removed any DC offset. The low gain channel used the same passive electronics, but included a pi-pad attenuator, which attenuated the incoming signal voltage approximately by a factor of five.

The DAQ used the CODA [25] readout software developed at Jefferson Lab to interface with the Single Board Computer (SBC) in the VME crate. It also used a JLab TI (trigger interface) board [26] to trigger the readout of an event.

The DAQ detected an ideal o-Ps event as follows: The beta decay of ^{22}Na was accompanied by the prompt emission of a 1.27 MeV gamma ray (branching ratio 99.940%), which provided the common start signal for the TDC and gates for the QDCs upon interacting in a NaI(Tl) bar. The stop signals were provided by the gamma rays emitted in the subsequent decay of the o-Ps. Several sets of delay lines provided synchronization between signals in the DAQ. In the event of an ideal o-Ps decay, three bars would register a stop time in a range determined by the mean lifetime of positronium plus the time it took for signals to pass through the delay line. In our case, we required that only two bars register a stop time in this same interval, because we were not very sensitive to the lowest energy gamma ray, $\vec{k}_3$, due to thresholds.

The charge deposited in individual bars was recorded using a QDC. In the case of an o-Ps event, at least two hits would be detected after the start signal with an energy that sums to less than 1022 keV. Gates for the QDC were generated using a CFD and sent down delay lines of sufficient length to align their respective charge pulses. The trigger system relied on the 'data ready' and 'busy' signals from each CAEN module. The busy signals from these cards were OR-ed in a logic gate, the output of which was used to veto any incoming signals while the DAQ was busy processing a previous event. The data ready signals from the three QDCs and TDC were OR-ed with a logic gate and sent to the trigger interface board, serving as the master trigger for prompting the

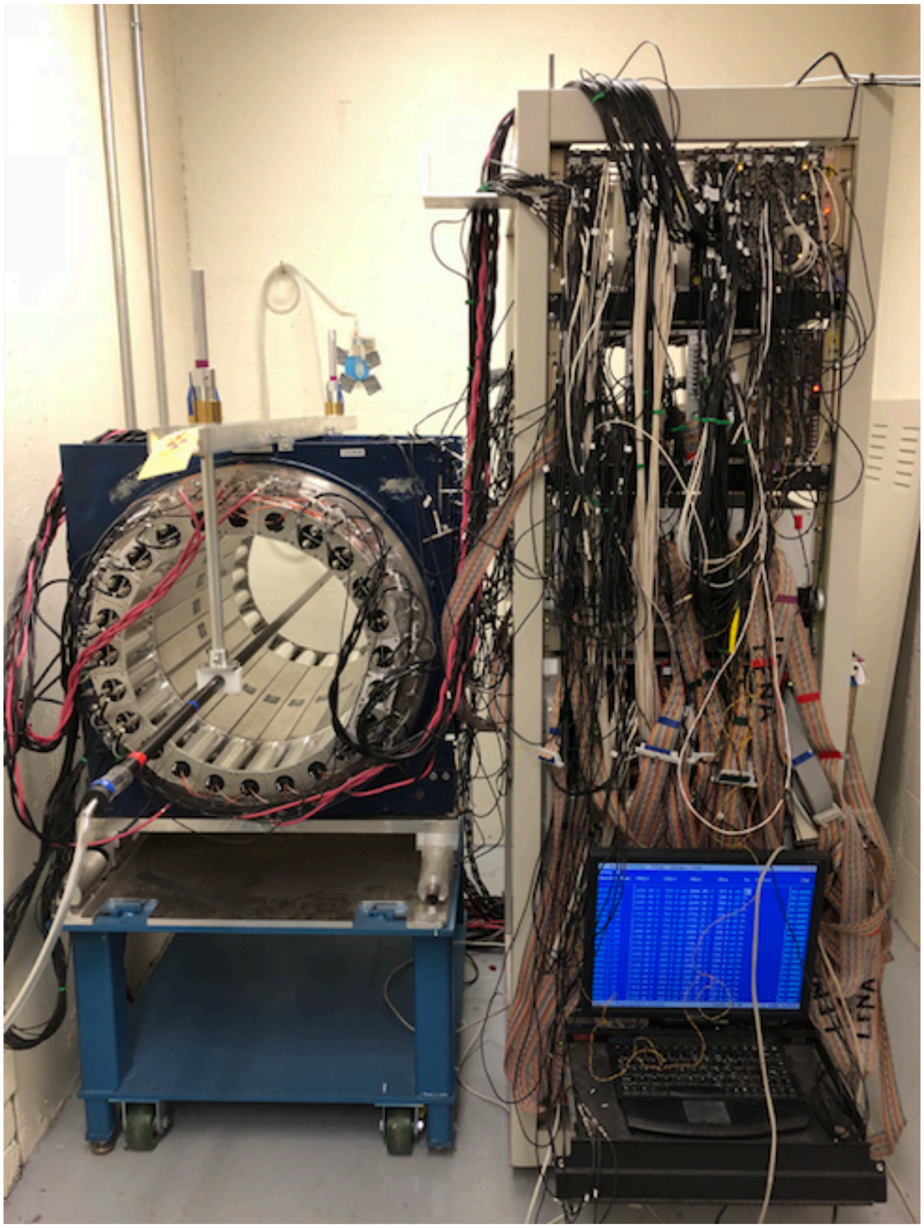

Figure 4: The APEX array equipped with the carbon fiber tube and tubing leading to the nitrogen tank (on the left). This tubing is hooked up to a bubbler on the back wall. On the right is the DAQ and the computer that controls the PMT voltages.

event readout. The data ready signals from individual QDC and TDC cards were recorded.

During data acquisition, a new run started every half hour, resulting in raw binary files 2.6 GB in size. These files were then immediately converted via the coda2root software from JLab [27] before being copied to data storage on UNC's Longleaf cluster for analysis. The Longleaf cluster is a Linux-based computing system with over 10,000 computing cores [28]. It is optimized for large quantities of jobs that do not require parallel processing. Once on the cluster, we further reduced the size of the files with code that removed all zeros from the data. This resulted in files that were each about 1 GB in size, that could be analyzed with ROOT [29]. A photo of the experiment during data acquisition can be seen in Fig. 4.

4. Event Reconstruction

Obtaining a clean sample of o-Ps decay events requires position and timing reconstruction of the gamma-rays emitted in the ^{22}Na source and subsequent o-Ps decays. The azimuthal angle of a gamma-ray interaction is simply given by the index of the bar, but the other information requires more sophisticated event reconstruction. The scheme presented here assumes a single interaction and is based on earlier work from [18, 23].

4.1. Energy Reconstruction

A simplified diagram of a single APEX bar after a gamma ray interaction is shown in Fig. 5 for reference. The light yield of a single pulse at one end of the bar can be modeled assuming exponential attenuation of the scintillation light as it propagates in the bar. Let μ be the attenuation coefficient, L the length of the bar, P the quantum efficiency of the PMT, E_γ the energy deposited by the gamma ray, z the position along the length of the NaI(Tl) bar, and E_0 the energy deposited per light photon created in the scintillator:

$$A_1 = \frac{E_\gamma P}{E_0} \exp(-\mu(L/2 + z)) \tag{1}$$

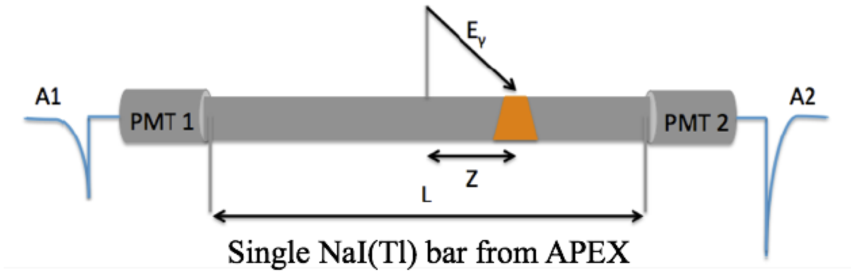

Figure 5: Event reconstruction in a single APEX Bar. A_1 and A_2 are the pulse amplitudes from the back and front bars, respectively. Z is the location of a gamma ray interaction along the length of the bar. L is the total length of the bar, 55 cm. E_γ is the energy deposited by a gamma ray interacting in the bar.

Similarly, the amplitude of the pulse at the opposite end of the bar can be expressed as:

$$A_2 = \frac{E_\gamma P}{E_0} \exp(-\mu(L/2 - z)) \tag{2}$$

The energy of the hit can then be determined via the two amplitudes [30]:

$$E_\gamma \propto \sqrt{(A_1 * A_2)}. \tag{3}$$

The proportionality constant was evaluated in the energy calibration process, which is described in subsequent sections.

4.1.1. Position Reconstruction

The location of an interaction along the length of a bar (z) can be reconstructed using the natural log of the ratio of the two PMT pulse amplitudes:

$$Z \propto \ln\left(\frac{A_1}{A_2}\right) \tag{4}$$

The proportionality constant was determined via the position calibration process, similar to the energy reconstruction.

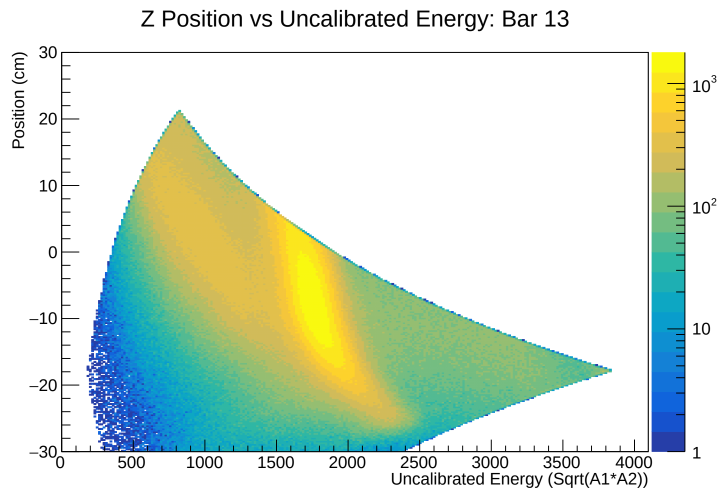

Figure 6: Z vs uncalibrated energy using the high gain channel for the front PMT and low gain channel for the back PMT for bar 13. The brightest yellow band corresponds to the 511 keV peak. The residual dependence of the energy is clearly visible.

4.1.2. Combining Information from High and Low-Gain Channels

Both high and low gain channels were used in order to improve the dynamic range of the array. Because the APEX array [18] is composed of relatively long bars, high energy hits towards the end of one bar (1.27 MeV) resulted in one QDC channel saturating. Furthermore, low energy events interacting at one end of the bar were significantly attenuated by the time they reached the opposite end. Information was combined from both high and low gain channels in order to take advantage of the full range of the DAQ and length of a bar.

In order to reconstruct the energy or position of a hit, a non-zero, non-saturated charge deposition had to be measured with the QDC for both the front and back PMT. As long as a pulse was obtained in either the high or low gain channel for both the front and back PMTs, it was possible to perform the event reconstruction. There were four possible options for an event reconstruction: 1) use the high gain channels for the front and back PMTs 2) use the low gain channels for the front and back PMTs 3) use the high gain channel for the front PMT and 4) use the low gain channel for the back PMT. Such channel combinations as described in 3) and 4) enabled us to detect events closer to the ends of the bars. Furthermore, the uncalibrated energy ($\sqrt{A_1 * A_2}$) had a residual dependence on the z position. This can be seen in Fig. 6. Therefore, the energy was calibrated in five different regions along the length of the bar, referred to as voxels: from -15 cm to -9 cm, -9 cm to -3 cm, -3 cm to +3 cm, +3 cm to +9 cm, and +9 cm to +15 cm. The usable length of a given bar depends on the channels used and the energy of the gamma ray, but in general the PMTs start to saturate between 10-15 cm.

4.2. Z Position Calibration

We calibrated the APEX array as follows: First, we calibrated the z position using a 10 μCi ^{22}Na source placed in a collimator consisting of two lead disks with a narrow gap in which to hold the activity.

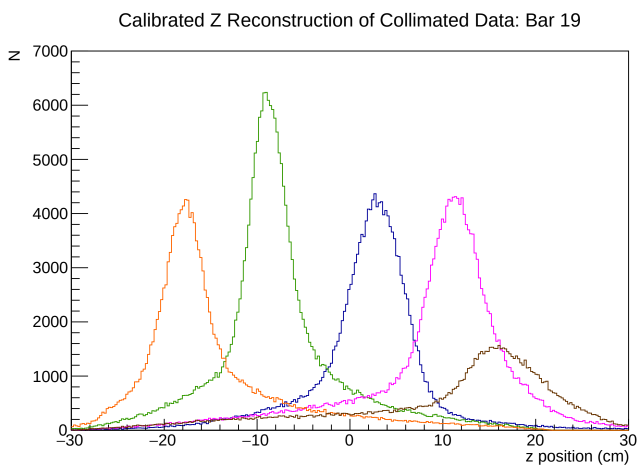

Figure 7: Position reconstruction with APEX array using 10 μCi collimated ^{22}Na source for a single bar. Shown are data sets taken with the collimated located at different positions inside the array. The z-positions of the source runs are, from left to right, -20cm, -10cm, 0cm, 10cm, 20cm. The z position reconstruction is not as good near the ends of the NaI(Tl) bars due to saturation and attenuation effects. This does not have much effect on our analysis, as z position reconstruction is not critical for identifying o-Ps in our data.

The lead disks constrained the gamma ray emissions to a single plane within the detector that was perpendicular to the axis of symmetry. Once inserted into

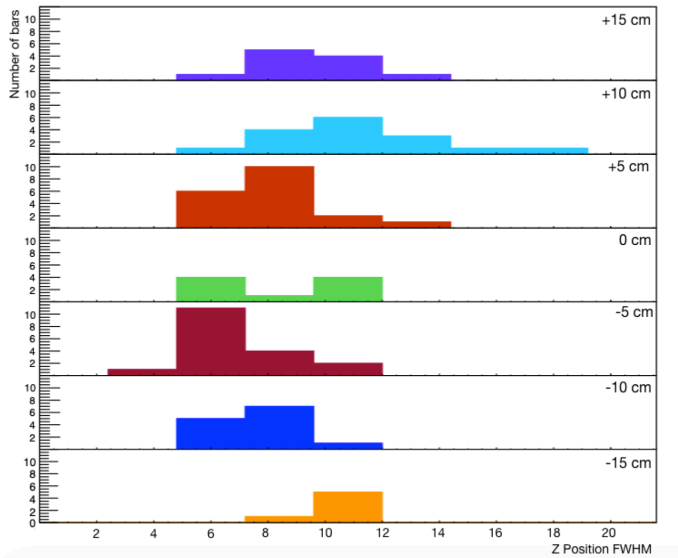

Figure 8: Z position resolution using the 511 keV gamma ray from ^{22}Na for different locations along the bar using the front high gain, back high gain channels. Some bars did not have good efficiency or would saturate near the end points, which explains why there are fewer bars histogrammed in these regions. If we could not perform a good fit of the collimated z position in that region of the bar, we did not use the data.

a cylindrical container, the lead collimator could be positioned within the array via a metal rod inscribed with markings every 0.5 cm. We placed this entire apparatus inside a long aluminum pipe that could be rolled into the APEX array along tracks. By adjusting the position of the pole, we could position the source along the z-axis of the array to within 0.5 cm. The slit width of the collimator was approximately 2 mm.

We performed the calibration by reconstructing the z position with Eq. 4 and fitting a line between the data acquired at 0 cm, ± 5 cm, ± 10 cm, and ± 15 cm for each bar. A few bars lacked sensitivity closer towards the PMTs, and so those data points were omitted from the fit if saturation of the PMT was a concern. All bars used at least four data points for the fit. While it may be relevant to potential o-Ps physics experiments, the z position reconstruction does not impact our ability to detect o-Ps. An example of the reconstructed z

position with the collimated ^{22}Na at different points within APEX can be seen in Fig. 7. The calibration was performed using all combinations of high and low gain channels for each bar, enabling us to reach a broader range of energies than possible otherwise. A plot showing the position resolution at different locations along the length of the bar can be seen in Fig. 8.

4.3. Energy Calibration

Previous APEX users have shown that there is a dependence of the energy on the z position for any given gamma ray interaction [30]. We were able to demonstrate this in Fig. 6. Furthermore, the specific z dependence is somewhat bar-dependent. To mitigate the effect of z-position on energy, we calibrated the energy separately using all possible high and low gain channel combination for five different voxels along the length of the bar. Using three uncollimated sources, we performed a linear fit between the two most salient peaks in each voxel. Depending on the bar and voxel, we either used the 511 keV peak in ^{22}Na and the 356 keV peak in ^{133}Ba, or the 511 keV peak in ^{22}Na and the 662 keV peak in ^{137}Cs. Multiple sources were necessary because the barium peak was too low in energy to perform a fit for four of the bars. In a CP- or CPT-violation search, this would limit our sensitivity to $\vec{k_2}$ gamma rays. We found the percent energy resolution for the 511 keV line in ^{22}Na was around 33% for the summed energy spectrum of all operational bars. The percent energy resolution for the 356 keV line in ^{133}Ba was about 50% for the summed energy spectrum. A histogram of the ^{22}Na percent energy resolutions for all bars in 5 different positions along the z axis of the detector are shown in Fig. 9. Additionally, the summed energy spectrum for all operational bars is shown for ^{133}Ba and ^{22}Na in Figs. 10 and 11, respectively. Improvements to this energy resolution would be necessary to perform a sensitive search for symmetry violations with APEX. One way to calculate the reduction in sensitivity that occurs as a result of having finite energy resolution is to calculate the probability of flipping the $\vec{k_1}$ and $\vec{k_2}$ gamma rays and weight them by the number of events for every possible pair of bars. Using this technique, we estimate that this would reduce our overall

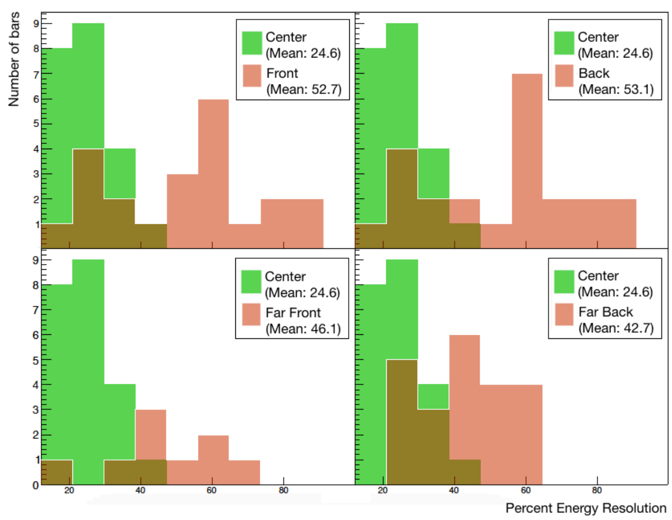

Figure 9: Percent energy resolution for different locations along the bar. Each canvas compares a different z voxel to the center voxel. 'Center' refers to interactions occurring between -3 cm and +3 cm. 'Front' refers to interactions occurring between +3 cm and +9 cm. 'Back' refers to interactions occurring between -3 cm and -9 cm. 'Far front' refers to interactions occurring between +9 cm and +15 cm. 'Far back' refers to interactions occurring between -9 cm and -15 cm. The poor energy resolution near the ends of the bar would impact our ability to distinguish between $\vec{k_1}$ and $\vec{k_2}$ gamma rays closer to the ends of the bar, which is necessary for a CP- or CPT-violation search, but not for confirmation of o-Ps detection.

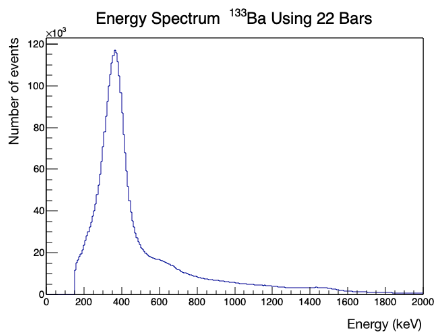

Figure 10: Summed energy spectrum from the 22 operational NaI(Tl) bars using an uncollimated, 1 μCi ^{133}Ba button source.

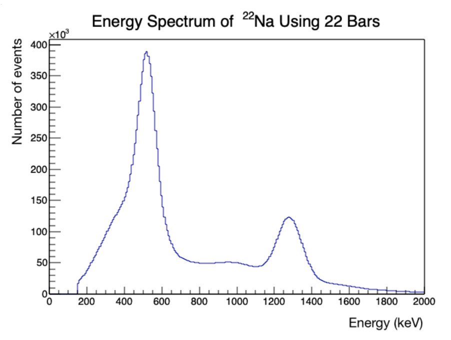

Figure 11: Summed energy spectrum from the 22 operational NaI(Tl) bars using an uncollimated, 10 μCi ^{22}Na button source.

sensitivity to CP- or CPT-violation by a factor of about 1.5.

4.4. Timing Reconstruction

The timing reconstruction ability of the DAQ was verified by using a pulser. The time interval measured was incrementally changed by adjusting the length of the cable running to the common start. By lengthening this cable, the time between the start and stop signal was shortened, as predicted. Using a pulser, we achieved a timing resolution between the detection of a 1.27 MeV gamma-rays and the subsequent o-Ps gammas of about 2 ns. In order to confirm o-Ps detection, we had to account for timing discrepancies between channels. We identified a characteristic delay time for each channel by looking at timing data acquired only with a single bar. The raw timing spectrum for an individual bar had a sharp, single bin peak, which represented the time difference between the arrival of the common start signal and the arrival of that same channel's individual stop signal. An example of this raw timing data can be seen in Fig. 12. At the beginning of the analysis, this value was subtracted from any raw timing values, enabling retroactive synchronization between the bars.

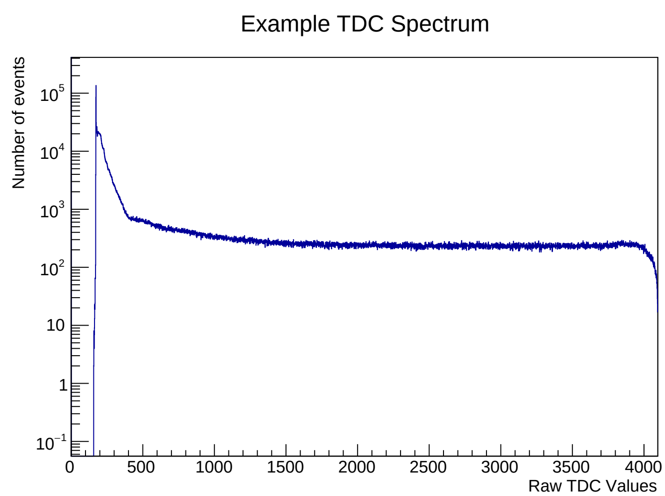

Figure 12: Example of a TDC spectrum using a ^{22}Na from a single bar. The spike is indicative of events for which the start and stop signal came from the same bar. This was confirmed via a pulser injected into only the channel for that bar.

5. Positronium Detection

5.1. o-Ps Detection

We confirmed the detection of o-Ps by comparing the timing spectra acquired with and without the aerogel. With aerogel, we were able to identify a timing component consistent with o-Ps decay. In the test without the aerogel, the aerogel was replaced with a thin aluminum disk to support the fragile source. In this section, we estimate our efficiencies and explain the motivation of all our analysis cuts.

The total efficiency of our detector can be estimated by taking a number of factors into account. These include the branching ratio of ^{22}Na, the solid angle of the aerogel as seen by the source, depolarization effects on the positron, the solid angles as seen by the different gamma rays, as well as the detection efficiencies. A critical factor is the efficiency for tagging the the 1.2 MeV gamma ray, which we estimated to be about 0.4, taking into account the solid angle and detection efficiencies of the bar. Overall, we estimated a total efficiency of about 7.9×10^{-4}. Estimations of the 1.2 MeV detection efficiency come from the solid angle calculation based on when the 1.2 MeV gamma ray saturates the PMT (it starts to saturate beyond ± 10 cm). The solid angle as seen by the o-Ps gamma rays was calculated in the same way. Not counting systematics, the sensitivity after one month, assuming no backgrounds, would be at the level of 4×10^{-5}. Our estimate of the efficiency was higher than what we measured it to be. The discrepancy could possibly be attributed to the DAQ or poor energy thresholds. This would warrant further investigation in the event of a search for CP- or CPT-violation. The most recent search for CP-violation in o-Ps had a statistical sensitivity of ± 0.0021 [16]. The most recent search for CPT-violation in o-Ps had a statistical sensitivity of ± 0.0031 [15]. While the estimated sensitivity sounds promising, it is important to consider that systematic effects may be dominant and difficult to minimize. Furthermore, the dead-time for a single event was about 7 μs, accounting for a 1 μs gate and 6 μs digitization time for the QDCs. From this information, we estimated a pile-up rate around 14%. We confirmed this pile-up in our data set by examining our timing spectra beyond 600 ns. We compared 'background' data (acquired with only the ^{22}Na source), with 'o-Ps' data (acquired with the ^{22}Na source and aerogel) and found that a flat background persisted in this region at the same level for both data sets. In the o-Ps case, this background constituted 14% of the total data acquired, and was consistent with pile-up. This is discussed further in Sec. 5.1.1. The requirements for an event to be flagged as an o-Ps event are shown in Table 1.

5.1.1. Analysis Cuts

We used the ROOT [29] software for the analysis, which involved the following cuts. First, we retained only events with three and four bar interactions. Three bar events typically account for $\vec{k_1}$, $\vec{k_2}$ and the 1.27 MeV gamma ray, whereas four bar events typically account for the $\vec{k_1}$, $\vec{k_2}$, and $\vec{k_3}$, and 1.27 MeV gamma ray. It is possible for such events to also consist of some Compton-scattered gamma rays, but this does not preclude us from demonstrating o-Ps detection by generating a timing spectrum. Furthermore, we have applied cuts

Number of bars, N	$2 < N < 5$
Start time, t_S	0 ns $< t_S <$ 40 ns
Start energy, E_S	1.1 MeV $< E_S <$ 1.6 MeV
$\vec{k_1}$ energy, E_1	330 keV $< E_1 <$ 511 keV
$\vec{k_2}$ energy, E_2	250 keV $< E_2 <$ 511 keV
Energy difference, ΔE_{12}	$\Delta E_{12} <$ 200 keV
Azimuthal angle, α	$110 < \alpha < 180$
Time difference Δt_{12}	$\Delta t_{12} <$ 40 ns
Z Position of k_1 (z_1)	-15 cm $< z_1 <$ +15 cm
Z Position of k_2 (z_2)	-15 cm $< z_2 <$ +15 cm

Table 1: Table showing requirements for an o-Ps event.

that seek to minimize Compton-scatters in our data set. Next, we applied a cut on the start time (t_S) and start energy (E_S), such that 0 ns $< t_S <$ 40 ns and 1.1 MeV $< E_S <$ 1.6 MeV. We defined the start time, t_S, as the time between when the start signal (1.27 MeV gamma ray) arrives and the delayed stop signal arrives. This cut is delineated by the black box shown in Fig. 13. We followed this with a cut on the $\vec{k_1}$ and $\vec{k_2}$ energies (E_1 and E_2) that was motivated by their theoretically predicted energy ranges: 330 keV $< E_1 <$ 511 keV and 250 keV $< E_2 <$ 511 keV. The theoretically predicted energy spectrum for the $\vec{k_1}$ and $\vec{k_2}$ gamma rays, as determined by Ore and Powell [31], can be seen in Figs. 14-15. Additionally, we implemented a cut on the difference between the $\vec{k_1}$ and $\vec{k_2}$ energies (ΔE_{12}) such that ΔE_{12} <200 keV. These cuts on the $\vec{k_1}$ and $\vec{k_2}$ energies reduced the number of Compton-scattered gamma rays in our final data set.

We further constrained the data set by requiring that the $\vec{k_1}$ and $\vec{k_2}$ gamma rays were within 40 ns of each other. This was proven to be long enough to account for timing differences due to different CFDs and lengths of cable. The 2D histogram of t_1 and t_2 can be seen in Fig. 17. Because the kinematics of o-Ps decay are known, we also imposed cuts based on the azimuthal angle between

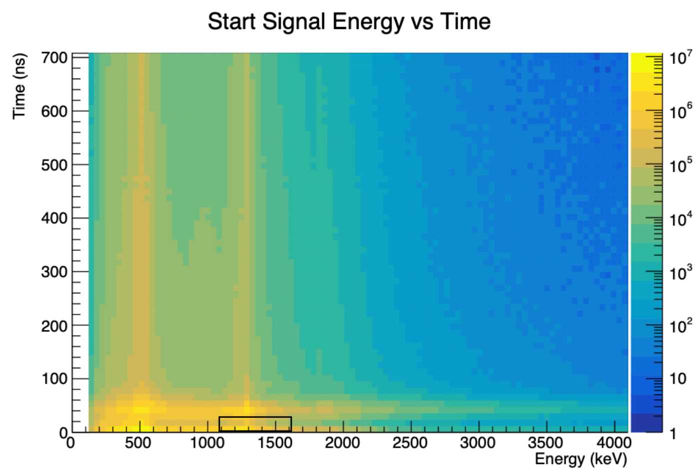

Figure 13: Start signal energy (x-axis) vs time (y-axis). The start signal is determined by the earliest hit time in the detector for a given event. The 511 keV gamma rays and 1.27 MeV gamma ray can be seen as yellow vertical bands due to pile-up. The earliest horizontal band are the events that trigger data acquisition. The second earliest horizontal band are events that are a result of o-Ps decay. We make two cuts on this histogram to isolate the 1.27 MeV start signal: one on the energy in the range (1.1 MeV to 1.6 MeV) and another on the time, (40-100 ns). This is delineated by the black box.

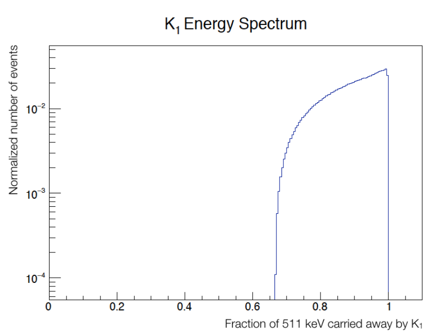

Figure 14: Predicted $\vec{k_1}$ energy distribution from o-Ps decay (simulation).

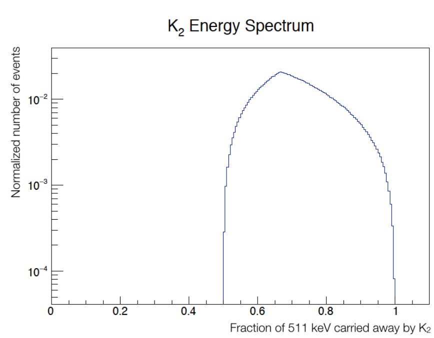

Figure 15: Predicted $\vec{k_2}$ energy distribution from o-Ps decay (simulation).

$\vec{k_1}$ and $\vec{k_2}$, α, shown in Fig. 16. Though our timing cut removes most p-Ps from our data set due to a factor of 1,000 difference in the mean lifetimes of p-Ps and o-Ps, some p-Ps inevitably remains due to pile-up. If one of the gamma rays scatters in a pile-up event, it is possible that such an event could be misidentified as o-Ps. The cut on the azimuthal angle rejected any events with back-to-back gamma rays from p-Ps decays, as it removes events with bars on opposite sides of the array. That said, it is still possible that more complex scattering patterns occurred and were misconstrued as o-Ps. For example, one gamma ray could exit the detector, and the other could scatter. We measured a flat background in our timing spectrum both with and without aerogel, extending out to 1 μs, which can be attributed to such events. Using this data, we estimated that such events comprise less than 15% of the total acquired o-Ps data. The last cuts in our analysis included a cut on the z position of $\vec{k_1}$ and $\vec{k_2}$ interactions and a cut on the average of t_1 and t_2 hit times. This final timing cut reduced pile-up in our detector. We also omitted two bars in our analysis. One bar was omitted because we did not have enough functional QDC channels to perform the event reconstruction. The other bar was omitted because the light collection of the PMT on one end was so poor as to render event reconstruction unfeasible.

We generated a timing spectrum by histogramming the average of the $\vec{k_1}$ and $\vec{k_2}$ hit times for each event. Fig. 18 shows the timing spectrum of events which survive our analysis cuts in the case of aerogel in nitrogen purge gas (top curve), aerogel in air (middle curve), and no aerogel (bottom curve). ROOT [29] was used to perform an exponential plus flat background fit to the middle and top curves (shown above). The middle curve was fit in the region from 70-500 ns and yielded a mean lifetime of 63$\pm$16 ns. The top curve was fit in the region from 70-600 ns and yielded a mean lifetime of 128$\pm$32 ns. This is consistent with the mean lifetime of o-Ps in nitrogen of 129.1$\pm$1.8 ns and the mean lifetime of o-Ps in air (80.1$\pm$2.6 ns) [21]. Although others have developed the ability to fit many more lifetime components in Ps timing spectra [14] [32], we believe that for our purposes, evidence of the long-lived component of about 129 ns is sufficient to demonstrate potential capabilities of the APEX array.

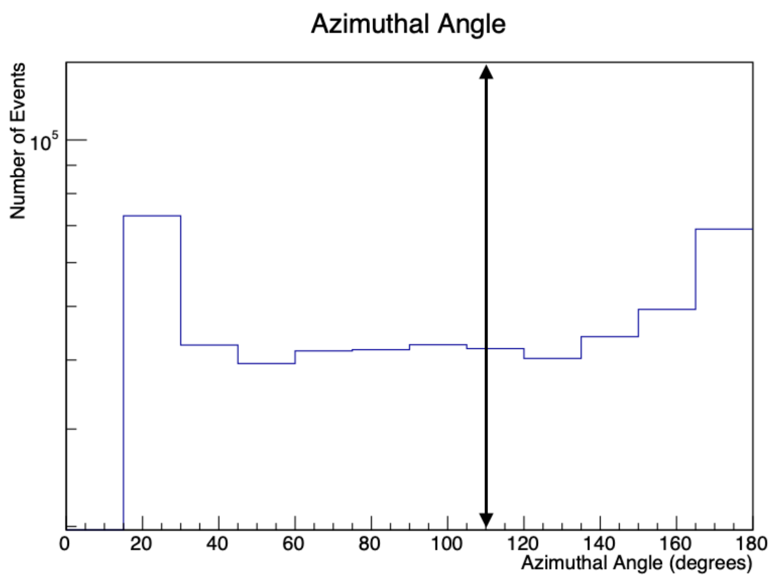

Figure 16: Azimuthal angle between $\vec{k_1}$ and $\vec{k_2}$ gamma rays. We accepted all events to the right of the black arrow.

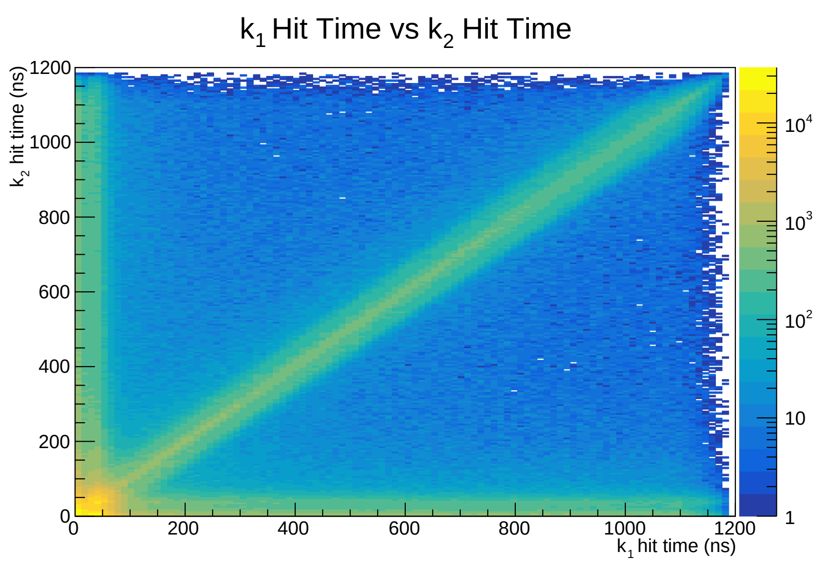

Figure 17: Histogram of the $\vec{k_1}$ and $\vec{k_2}$ hit times. We accepted all events for which the timing difference between $\vec{k_1}$ and $\vec{k_2}$ was less than 40 ns.

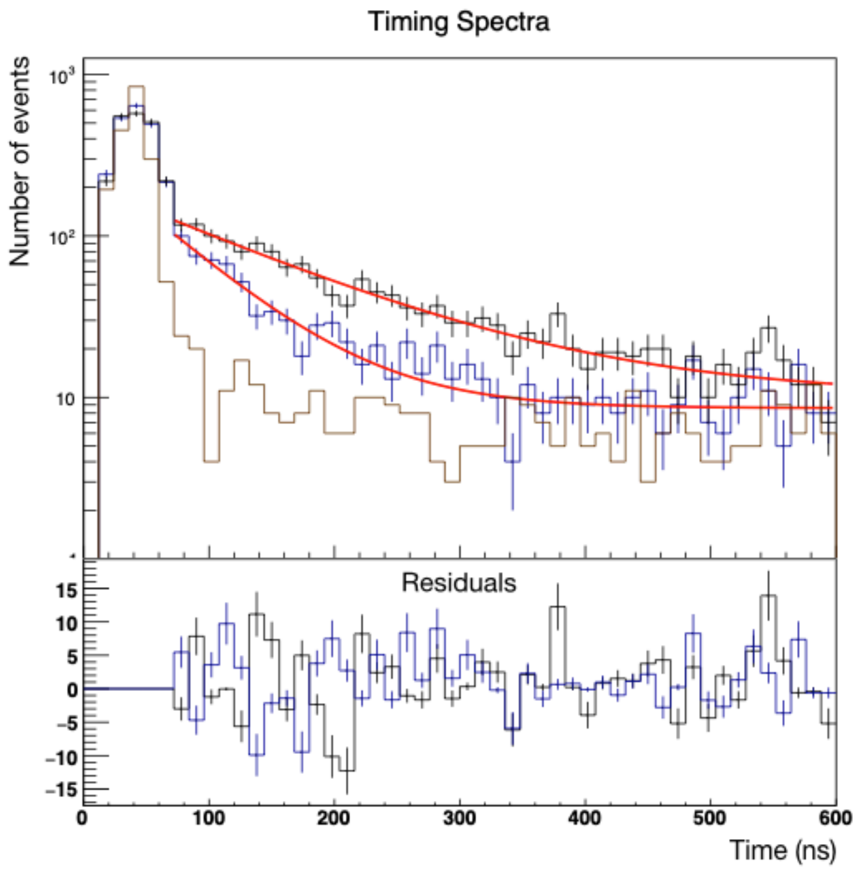

Figure 18: Timing Spectrum. The top curve indicates the data with aerogel and nitrogen purge gas, middle indicates the data with aerogel in air, and the bottom curve indicates the data taken with the aerogel replaced by a thin aluminum disk. A fit in the region from 70-600 ns for the top curve yielded a mean lifetime of 128±32 ns. This is consistent with the mean lifetime of o-Ps in nitrogen obtained by another group of 129.1 ns±1.8 [21]. A fit in the region from 70-600 ns for the middle curve yielded a mean lifetime of 63±16 ns. This is consistent with the mean lifetime of o-Ps in air obtained by another group of 80.1±2.6 ns [21].A chi-squared goodness of fit test was performed for both fits. In the case of nitrogen, we calculated χ^2/n, where n is the number of degrees of freedom, to be 1.04. In the case of air, we calculated it to be 1.24.

6. Conclusion

Using the APEX array, we have demonstrated o-Ps identification by tagging on the 1.27 MeV gamma ray in an array of NaI(Tl) detectors. This technique has the potential to simplify future experimental designs with the APEX array or similar detectors. Tagging on the 1.27 MeV gamma ray, as opposed to tagging on the positron, removes the need for excess material (scintillator and optical fiber) inside the source holder and detector. One potential benefit of this is a reduction of Compton-scattering of gamma rays. It also eliminates the need for an extra light sensor that triggers the DAQ. This allows for a simpler DAQ design and less complicated detector geometries. A unique feature of the APEX detector and DAQ is that any one of its bars can be used to tag on the 1.27 MeV gamma ray. Though the approach of tagging on the 1.27 MeV gamma ray has been used in PALS [1], we have broadened the technique to be used in arrays with high angular resolution, enabling its use in CP- and CPT-violation searches in o-Ps. Finally, our experiences with APEX suggest that increased light collection efficiency and a digitizer-based DAQ would improve the setup greatly, possibly enabling interesting searches for new physics in o-Ps. The light collection efficiency could likely be improved via the use of Silicon Photomultipliers (SiPMs) instead of PMTs. This would improve the energy resolution, particularly near the ends of the NaI(Tl) bars. The energy calibration technique could also be enhanced by using finer discretization along the z length of the bar when calibrating the energy, though this is only worthwhile if the light collection efficiency could first be improved. Such developments could lead to an effective search for fundamental symmetries in o-Ps.

Acknowledgments

The authors would like to acknowledge the TUNL staff, in particular engineers Matthew Busch and Brogan Thomas for the design of the carbon fiber tube support structure. Many thanks also go to Professor Mohammad Ahmed at Duke University for his support with the DAQ and Alex Crowell for his support with CODA and to Professor Art Champagne for the use of the APEX array. Additionally, the authors are grateful for input from Professor John Wilkerson at UNC Chapel Hill and his expertise on fundamental symmetry experiments. This material is based upon work supported by the U.S. Department of Energy, Office of Science, Office of Nuclear Physics under Awards No. DE-FG02-97ER41041 and No. DE-FG02-97ER41033. We would like to thank the University of North Carolina at Chapel Hill and the Research Computing group for providing computational resources and support that have contributed to these research results.

References

[1] D. W. Gidley, H.-G. Peng, R. S. Vallery, Positron annihilation as a method to characterize porous materials, Annu. Rev. Mater. Res. 36 (2006) 49–79.

[2] W. Bernreuther, O. Nachtmann, Weak Interaction Effects in Positronium, Z.Phys. C11 (1981) 235.

[3] L. Wolfenstein, D. G. Ravenhall, Some consequences of invariance under charge conjugation, Phys. Rev. 88 (1952) 279–282.

[4] G. S. Adkins, R. N. Fell, J. Sapirstein, Two-Loop Correction to the Orthopositronium Decay Rate, Annals of Physics 295 (2002) 136–193.

[5] R. S. Vallery, P. W. Zitzewitz, D. W. Gidley, Resolution of the orthopositronium-lifetime puzzle, Phys. Rev. Lett. 90 (2003) 203402.

[6] S. G. Karshenboim, Precision study of positronium: Testing bound state qed theory, International Journal of Modern Physics A 19 (2004) 3879–3896.

[7] S. Asai, O. Jinnouchi, T. Kobayashi, Solution of the Orthopositronium Lifetime Puzzle, International Journal of Modern Physics A 19 (2004) 3927–3938.

[8] A. Czarnecki, K. Melnikov, A. Yelkhovsky, Positronium s-state spectrum: Analytic results at $o(m\alpha^6)$, Phys. Rev. A 59 (1999) 4316–4330.

[9] A. H. Al-Ramadhan, D. W. Gidley, New precision measurement of the decay rate of singlet positronium, Phys. Rev. Lett. 72 (1994) 1632–1635.

[10] W. Bernreuther, U. Low, J. Ma, O. Nachtmann, How to Test CP, T and CPT Invariance in the Three Photon Decay of Polarized s Wave Triplet Positronium, Z.Phys. C41 (1988) 143.

[11] P. Crivelli, A. Belov, U. Gendotti, S. Gninenko, A. Rubbia, Positronium portal into hidden sector: a new experiment to search for mirror dark matter, Journal of Instrumentation 5 (2010) P08001–P08001.

[12] S. N. Gninenko, N. V. Krasnikov, V. A. Matveev, A. Rubbia, Some aspects of positronium physics, Physics of Particles and Nuclei 37 (2006) 321–346.

[13] Y. Nagashima, M. Kakimoto, T. Hyodo, K. Fujiwara, A. Ichimura, T. Chang, J. Deng, T. Akahane, T. Chiba, K. Suzuki, B. T. A. McKee, A. T. Stewart, Thermalization of free positronium atoms by collisions with silica-powder grains, aerogel grains, and gas molecules, Phys. Rev. A 52 (1995) 258–265.

[14] Y. Kobayashi, K. Ito, T. Oka, K. Hirata, Positronium chemistry in porous materials, Radiation Physics and Chemistry 76 (2007) 224 – 230. Proceedings of the 8th International Workshop on Positron and Positronium Chemistry.

[15] P. A. Vetter, S. J. Freedman, Search for *cpt*-odd decays of positronium, Phys. Rev. Lett. 91 (2003) 263401.

[16] T. Yamazaki, T. Namba, S. Asai, T. Kobayashi, Search for *cp* violation in positronium decay, Phys. Rev. Lett. 104 (2010) 083401.

[17] Mohammed, Muhsin, Gajos, Aleksander, The tests of cp and cpt symmetry using the j-pet detector, EPJ Web Conf. 199 (2019) 05027.

[18] M. Wolanski, S. Freedman, J. Dawson, W. Haberichter, K. Chan, A. Chishti, N. Kaloskamis, C. Lister, Trigger processor for the apex positron-electron spectrometer, Nuclear Instruments and Methods in Physics Research Section A: Accelerators, Spectrometers, Detectors and Associated Equipment 361 (1995) 326 – 337.

[19] J. Yang, M. Chiba, R. Hamatsu, T. Hirose, M. Irako, T. Kumita, Study on spin precession of polarized slow positrons in solids, Japanese Journal of Applied Physics 36 (1997) 3764–3769.

[20] E. . Ziegler, Eckert & ziegler, `http://www.ezag.com`, 2017.

[21] P. Crivelli, New Search for Invisible Decays of o-Ps, Ph.D. thesis, ETH Zurich, 2006.

[22] S. M. Daigle, Low Energy Proton Capture Study Of The $^{14}\mathrm{N}(p,\gamma)^{15}\mathrm{O}$ Reaction, Ph.D. thesis, University of North Carolina, Chapel Hill, 2013.

[23] S. Daigle, K. J. Kelly, A. E. Champagne, M. Q. Buckner, C. Iliadis, C. Howard, Measurement of the $E_r^{\mathrm{c.m.}} = 259$ kev resonance in the $^{14}\mathrm{N}(p,\gamma)^{15}\mathrm{O}$ reaction, Phys. Rev. C 94 (2016) 025803.

[24] CAEN, Costruzioni apparecchiature elettroniche nucleari s.p.a., `http://www.caen.it`, 2019.

[25] J. Lab, Coda, `https://coda.jlab.org/drupal/`, 2017.

[26] J. W. Gu, Description and Technical Information for the VME Trigger Interface (TI) Module, `https://coda.jlab.org/drupal/filebrowser/download/857072`, Jefferson Lab, 2018.

[27] A. Teymurazyan, Coda2root, `https://sites.google.com/site/codeforhigs/tunl-coda-file-parsing/coda2root-utility`, 2019.

[28] UNC, Longleaf, `https://its.unc.edu/research-computing/longleaf-cluster/`, 2019.

[29] R. Brun, F. Rademakers, ROOT: An object oriented data analysis framework, Nucl. Instrum. Meth. A389 (1997) 81–86.

[30] S. M. Daigle, Low Energy Proton Capture Study of the $^{14}N(p,\gamma)^{15}O$ Reaction, Ph.D. thesis, University of North Carolina, Chapel Hill, 2013.

[31] A. Ore, J. L. Powell, Three-photon annihilation of an electron-positron pair, Phys. Rev. 75 (1949) 1696–1699.

[32] Z. Kajcsos, L. Liszkay, G. Dupltre, L. Lohonyai, L. Varga, K. Lzr, G. Pl-Borbly, H. Beyer, P. Caullet, J. Patarin, A. Lima, C. Gil, P. Gordo, M. Marques, Positron and positronium in porous media: zeolites, Radiation Physics and Chemistry 68 (2003) 363 – 368. Proceedings of the 7th International Conference on Positron and Positronium Chemistry.